record size of the October 2015 ozone hole would hold based on our calculations even if the volcanic aerosol amounts were overestimated by a factor of several (a much larger error than indicated by our comparison of our model calculations with lidar data for multiple eruptions in (*26*); supplementary materials).

The reasons for the contributions of dynamics and temperature to the healing of the Antarctic ozone layer are not clear. The dynamical and temperature contributions to healing estimated in Fig. 3 vary by month in a manner that mirrors the ozone depletion in spring, suggesting linkages to the seasonality of the depletion itself and hence possible dynamical feedbacks. Some models (*33*–*35*) suggest that a reduction in transport of ozone to the Antarctic occurred as depletion developed in the 1980s and 1990s, which would imply a reversal of this process and hence increased healing as ozone rebounds. But others indicate that ozone depletion increased the strength of the stratospheric overturning circulation (*36*), and a reversal of this factor during recovery would impede healing. Although there is robust agreement across models that climate change linked to increasing greenhouse gases should act to increase the strength of the stratospheric overturning circulation, observations show mixed results (*37*); further, the seasonality of this effect has not been established, and the magnitude in the Antarctic is uncertain. Internal variability of the climate system linked, for example, to variations in El Niño could also affect the trends.

Conclusion

After accounting for dynamics, temperature, and volcanic factors, the results presented here indicate that healing of the Antarctic ozone hole is emerging. Our results underscore the combined value of balloon and satellite ozone data, volcanic aerosol measurements, and chemistry-climate models in documenting progress in the recovery of the ozone layer since the Montreal Protocol.

REFERENCES AND NOTES

1. J. C. Farman, B. G. Gardiner, J. D. Shanklin, *Nature* **315**, 207–210 (1985).
2. World Meteorological Organization/United Nations Environment Programme (WMO/UNEP), *Scientific Assessment of Ozone Depletion: 2014* (Global Ozone Research and Monitoring Project Report No. 55, WMO, 2014).
3. D. J. Hofmann, S. J. Oltmans, J. M. Harris, B. J. Johnson, J. A. Lathrop, *J. Geophys. Res.* **102**, 8931–8943 (1997).
4. M. J. Newchurch *et al.*, *J. Geophys. Res.* **108**, 4507 (2003).
5. N. R. P. Harris *et al.*, *Atmos. Chem. Phys.* **15**, 9965–9982 (2015).
6. F. Tummon *et al.*, *Atmos. Chem. Phys.* **15**, 3021–3043 (2015).
7. T. G. Shepherd *et al.*, *Nat. Geosci.* **7**, 443–449 (2014).
8. E.-S. Yang *et al.*, *J. Geophys. Res.* **113**, D20308 (2008).
9. M. L. Salby, E. Titova, L. Deschamps, *Geophys. Res. Lett.* **38**, L09702 (2011).
10. J. Kuttippurath *et al.*, *Atmos. Chem. Phys.* **13**, 1625–1635 (2013).
11. WMO, "WMO Antarctic Ozone Bulletins: 2015," 2015; www.wmo.int/pages/prog/arep/WMOAntarcticOzoneBulletins2015.html.
12. S. Solomon, *Rev. Geophys.* **37**, 275–316 (1999).
13. J. Kuttippurath *et al.*, *Atmos. Chem. Phys.* **15**, 10385–10397 (2015).
14. N. J. Livesey, M. L. Santee, G. L. Manney, *Atmos. Chem. Phys.* **15**, 9945–9963 (2015).
15. D. J. Hofmann, S. J. Oltmans, *J. Geophys. Res.* **98**, 18555–18561 (1993).
16. R. W. Portmann *et al.*, *J. Geophys. Res.* **101**, 22991–23006 (1996).
17. J.-P. Vernier *et al.*, *Geophys. Res. Lett.* **38**, L12807 (2011).
18. C. Brühl, J. Lelieveld, H. Tost, M. Höpfner, N. Glatthor, *J. Geophys. Res. Atmos.* **120**, 2103–2118 (2015).
19. R. D. McPeters, P. K. Bhartia, D. Haffner, G. L. Labow, L. Flynn, *J. Geophys. Res.* **118**, 8032–8039 (2013).
20. W. Chehade, M. Weber, J. P. Burrows, *Atmos. Chem. Phys.* **14**, 7059–7074 (2014).
21. D. R. Marsh *et al.*, *J. Clim.* **26**, 7372–7391 (2013).
22. A. Kunz, L. L. Pan, P. Konopka, D. E. Kinnison, S. Tilmes, *J. Geophys. Res.* **116**, D24302 (2011).
23. Materials and methods are available as supplementary materials on *Science* Online.
24. S. Solomon, D. Kinnison, J. Bandoro, R. R. Garcia, *J. Geophys. Res.* **120**, 7958–7974 (2015).
25. F. Arfeuille *et al.*, *Atmos. Chem. Phys.* **13**, 11221–11234 (2013).
26. M. J. Mills *et al.*, *J. Geophys. Res.* **121**, 2332–2348 (2015).
27. M. Höpfner *et al.*, *Atmos. Chem. Phys.* **15**, 7017–7037 (2015).
28. P. A. Newman, E. R. Nash, S. R. Kawa, S. A. Montzka, S. M. Schauffler, *Geophys. Res. Lett.* **33**, L12814 (2006).
29. A. A. Scaife *et al.*, *J. Atmos. Sci.* **62**, 629–639 (2005).
30. P. M. Forster, R. S. Freckleton, K. P. Shine, *Clim. Dyn.* **13**, 547–560 (1997).
31. B. Hassler, G. E. Bodeker, S. Solomon, P. J. Young, *Geophys. Res. Lett.* **38**, L01805 (2011).
32. A. Tabazadeh, K. Drdla, M. R. Schoeberl, P. Hamill, O. B. Toon, *Proc. Natl. Acad. Sci. U.S.A.* **99**, 2609–2612 (2002).
33. S. Meul, S. Oberländer-Hayn, J. Abalichin, U. Langematz, *Atmos. Chem. Phys.* **15**, 6897–6911 (2015).
34. P. Braesicke *et al.*, *Atmos. Chem. Phys.* **13**, 10677–10688 (2013).
35. F. Li, J. Austin, J. Wilson, *J. Clim.* **21**, 40–57 (2008).
36. C. McLandress, T. G. Shepherd, *J. Clim.* **22**, 1516–1540 (2009).
37. N. Butchart, *Rev. Geophys.* **52**, 157–184 (2014).

ACKNOWLEDGMENTS

We thank S. Tilmes (NCAR) for help with the MERRA (Modern-Era Retrospective Analysis for Research and Applications) data. D.K. and S.S. were partially supported by NSF Frontiers in Earth System Dynamics grant OCE-1338814, and D.J.I. was supported by NSF Atmospheric Chemistry grant AGS-1539972. A.S. was supported by an Academic Research Fellowship from the University of Leeds, an NCAR visiting scientist grant, and Natural Environment Research Council grant NE/N006038/1. NCAR is sponsored by NSF. WACCM is a component of CESM, which is supported by NSF and the Office of Science of the U.S. Department of Energy. We are grateful to D. Fahey, B. Hassler, W. D. McKenna, and the anonymous reviewers for helpful comments. Instructions for access to data reported in this paper are given in the supplementary materials.

SUPPLEMENTARY MATERIALS

www.sciencemag.org/content/353/6296/269/suppl/DC1
Materials and Methods
Figs. S1 to S4
Tables S1 to S3
References (*38*–*44*)

6 December 2015; accepted 20 June 2016
Published online 30 June 2016
10.1126/science.aae0061

REPORTS

FERROELECTRICITY

Discovery of robust in-plane ferroelectricity in atomic-thick SnTe

Kai Chang,[1,2]* Junwei Liu,[3,1,2]* Haicheng Lin,[1,2] Na Wang,[1,2] Kun Zhao,[1,2] Anmin Zhang,[4] Feng Jin,[4] Yong Zhong,[1,2] Xiaopeng Hu,[1,2] Wenhui Duan,[1,2] Qingming Zhang,[4,5] Liang Fu,[3] Qi-Kun Xue,[1,2] Xi Chen,[1,2]† Shuai-Hua Ji[1,2,6]†

Stable ferroelectricity with high transition temperature in nanostructures is needed for miniaturizing ferroelectric devices. Here, we report the discovery of the stable in-plane spontaneous polarization in atomic-thick tin telluride (SnTe), down to a 1–unit cell (UC) limit. The ferroelectric transition temperature T_c of 1-UC SnTe film is greatly enhanced from the bulk value of 98 kelvin and reaches as high as 270 kelvin. Moreover, 2- to 4-UC SnTe films show robust ferroelectricity at room temperature. The interplay between semiconducting properties and ferroelectricity in this two-dimensional material may enable a wide range of applications in nonvolatile high-density memories, nanosensors, and electronics.

Two-dimensional (2D) materials exhibit a wide range of symmetry-breaking quantum phenomena such as crystalline order (*1*, *2*), superconductivity (*3*, *4*), magnetism (*5*, *6*), and charge-density wave (*7*, *8*), which persist in the limit of a single-unit-cell thickness. It has been comparatively more difficult to explore ferroelectricity in ultrathin films. For the perovskite ferroelectric materials, stable out-plane spontaneous polarization has been discovered in the thin films of few unit cells (UCs) thickness (*9*–*12*). Theoretical studies point out that the charge screening, chemical bonding, and misfit strain at the interface may play a role in stabilizing ferroelectric states (*13*–*18*). The transition temperature in those ultrathin films usually decreases as the thickness is reduced (*10*–*12*, *19*), which could be understood by the destabilization of ferroelectric states through depolarization fields. In contrast, the transition temperature of ferroelectric polymer film is nearly independent of thickness, indicating 2D behavior (*20*).

Here, we use the molecular beam epitaxial technique to prepare atomic-thick ferroelectric

SnTe films and discover stable in-plane spontaneous polarization in SnTe film of only one UC thickness, 0.63 nm. To avoid external strain effect, we employ the graphitized 6H-SiC(0001) substrate in epitaxial growth to obtain stress-free thin films. The substrate surface is mainly covered by the monolayer/bilayer graphene. The weak van der Waals bonding between substrate and SnTe film largely reduces the strain effect and helps to preserve the in-plane component of the polarization.

[1]State Key Laboratory of Low-Dimensional Quantum Physics, Department of Physics, Tsinghua University, Beijing 100084, China. [2]Collaborative Innovation Center of Quantum Matter, Beijing 100084, China. [3]Department of Physics, Massachusetts Institute of Technology, Cambridge, MA 02139, USA. [4]Department of Physics, Beijing Key Laboratory of Optoelectronic Functional Materials and Micro-Nano Devices, Renmin University of China, Beijing 100872, China. [5]Collaborative Innovation Center of Advanced Microstructures, Nanjing 210093, China. [6]RIKEN Center for Emergent Matter Science (CEMS), Wako, Saitama 351-0198, Japan.
*These authors contributed equally to this work. †Corresponding author. Email: xc@mail.tsinghua.edu.cn (X.C.); shji@mail.tsinghua.edu.cn (S.-H.J.)

In the bulk form, SnTe is a narrow-gap (~0.2 eV) semiconductor (*21*) and possesses the rock-salt structure with a lattice constant of 6.32 Å (Fig. 1A) at room temperature. SnTe is always heavily p-type doped because of the negative formation energy of Sn vacancy (*22*). At the ferroelectric transition temperature T_c, the crystal goes through a cubic-to-rhombohedral structural phase transition and the two sublattices of Sn and Te atoms are displaced from each other along the [111] direction, forming the ferroelectric state (*23*, *24*). Owing to the screening effect of charge carriers, T_c drops rapidly as the concentration of Sn vacancy increases (*25*), and the highest transition temperature of bulk SnTe is only 98 K (*26*). Recently, interest in the ferroelectric structural distortion in SnTe was rekindled by its effect on electronic properties of the topological crystalline insulator phase newly discovered in group IV-VI semiconductors (*27*).

The SnTe films grown on SiC are characterized by the in situ reflection high-energy electron diffraction (RHEED) [(*28*), fig. S1] and scanning tunneling microscopy (STM) topography images (Fig. 1B and fig. S1). At low coverage, (001)-oriented islands are formed on the substrate. In contrast to the case involving strong directional covalent bonds, the lattice-matching conditions are largely relaxed in the van der Waals epitaxy. As a consequence, the in-plane orientation of the SnTe islands is randomly distributed. The weak bonding is also demonstrated by the fact that an entire island at the size of 100 nm can be displaced by the STM tip (fig. S2). By carefully controlling the substrate temperature and SnTe flux, the size of an island can be as large as ~1 μm (fig. S1). The facet edges along the [100] and [010] directions are clearly seen in the STM images. The island thickness corresponds to an integer multiple of the SnTe unit cell (no half layer), which is consistent with the formation energy calculation (fig. S3). The topography images (fig. S4) also indicate that the formation of Sn vacancies is greatly suppressed in the atomic-thin SnTe films. The surface defect density is 10^{10} to 10^{11} cm^{-2} for the 2-UC film and even lower for

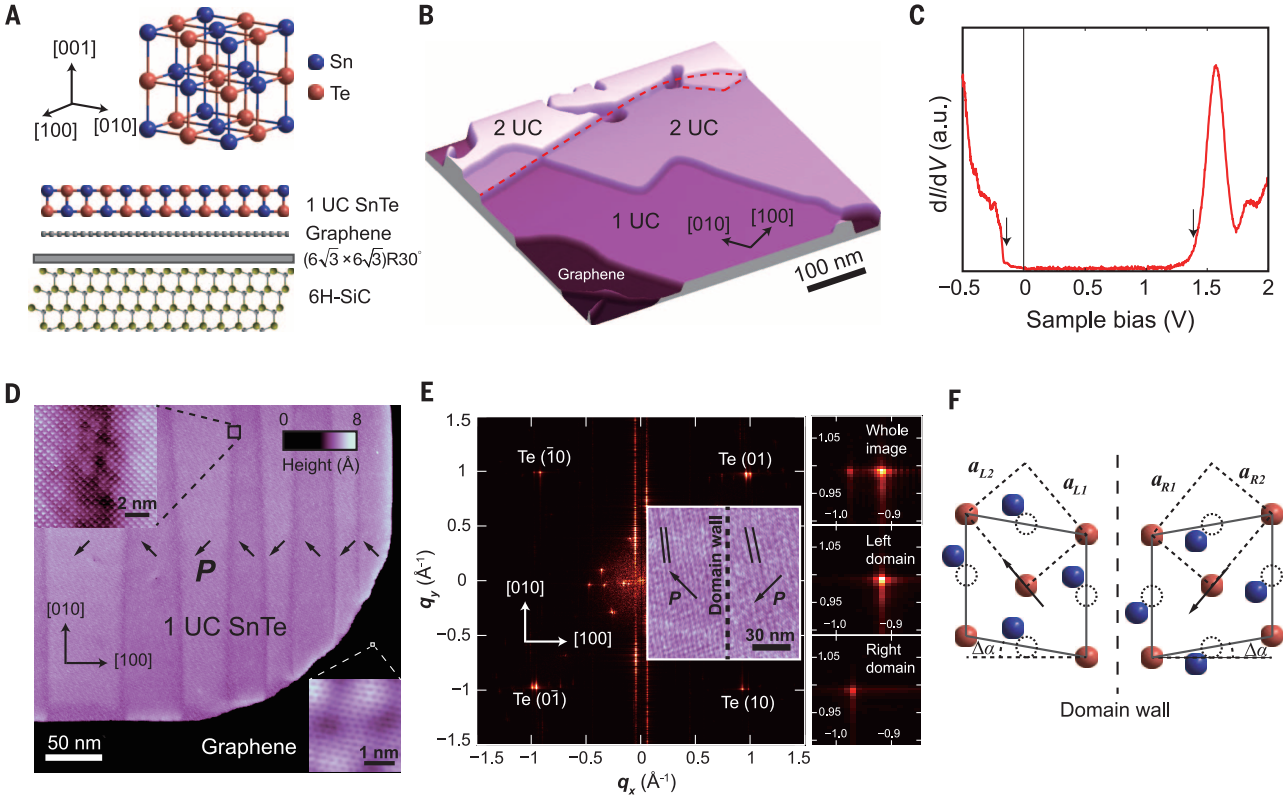

Fig. 1. Structure and lattice distortion of SnTe film. (**A**) Schematics of the SnTe crystal structure (upper) and the SnTe film (lower). (**B**) Typical STM topography image of SnTe film (sample bias 3.0 V, tunneling current 30 pA, temperature 4.7 K). The red dotted line indicates the steps of substrate. (**C**) The d*I*/d*V* spectra acquired on the surface of a 1-UC film at 4.7 K. The d*I*/d*V* of conduction and valence bands has large difference in intensity. For clarity, the spectra above and below the Fermi level are measured under different tunneling conditions: 3.0 V, 100 pA above and −0.5 V, 100 pA below. The arrows indicate the edges of the valence and conduction bands. The peak at 1.5 V corresponds to a van Hove singularity in the conduction band. (**D**) The stripe domain of a 1-UC SnTe film (imaging conditions: −0.2 V, 30 pA, 4.7 K). The arrows in each domain indicate the direction of lattice distortion. (Upper inset) Topography image across a domain boundary (−0.2 V, 100 pA). (Lower inset) The graphene substrate (−0.1 V, 200 pA). (**E**) Fourier transform (left) of an area (inset, 4.7 K) crossing a domain boundary. The Bragg peaks are associated with the Te sublattice. The parallel lines in the inset indicate the moiré stripes in each domain. The atomically resolved image right on the domain boundary is shown in fig. S5. The Te($\bar{1}$0) peaks for the whole image, the left domain, and the right domain are enlarged in the right panels. (**F**) Schematic of the lattice distortion and atom displacement in the ferroelectric phase. The solid lines indicate the rock-salt unit cell, and the dashed lines indicate the primitive cell of the Te sublattice. The arrows point to the directions of distortion. a_{L1}, a_{L2}, a_{R1}, and a_{R2} are the lattice constants of the Te sublattice, and $\Delta\alpha$ is the distortion angle of the rock-salt unit cell. For more details, see figs. S6 to S9.

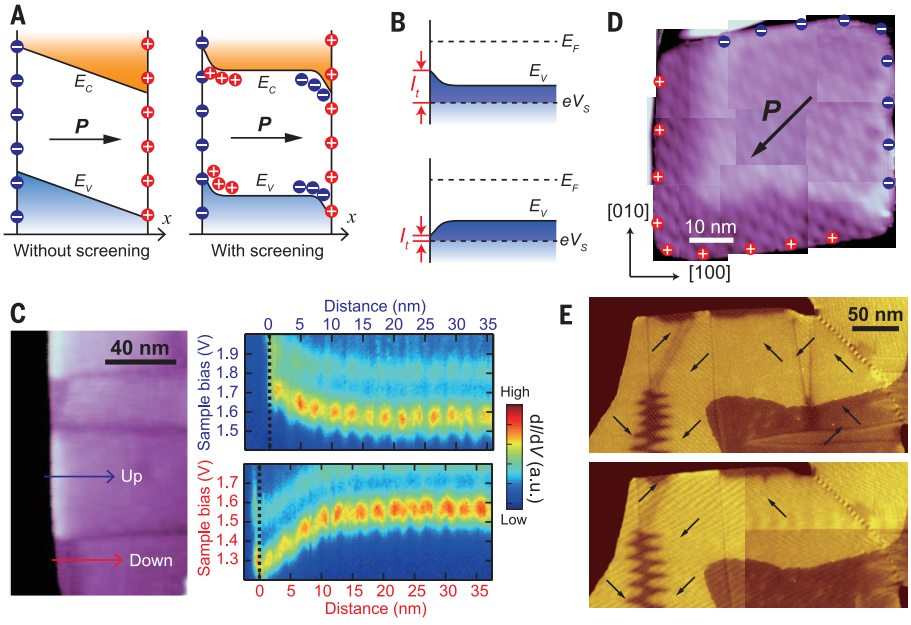

Fig. 2. Band-bending induced by spontaneous polarization and manipulation of the domain walls. (**A**) Schematics showing the band shift of a bulk ferroelectric with and without internal screening charge. (**B**) The apparent height of an edge. If an edge is negatively charged (top panel), more states between Fermi level (E_F) and the bias (eV_s) are available for tunneling. Therefore, the STM tip has to be lifted up to keep a constant current during scanning, giving rise to a higher apparent height. A positively charged edge has the opposite trend. (**C**) Spatially resolved d*I*/d*V* spectra (right panels) obtained along the two arrows in the image on the left (1 UC, 3.0 V, 100 pA, 4.7 K). A few typical d*I*/d*V* curves (near both conduction and valence band edges) and the fitting of the bending profiles are shown in figs. S11 and S12. (**D**) STM image of a 1-UC single-domain island (−0.2 V, 100 pA, 4.7 K). The polarization is unambiguously determined to be along the [$\bar{1}\bar{1}$0] direction. The image is a combination of nine smaller scans. The "+" and "−" signs on the edges indicate the positive and negative polarization charges. (**E**) Topography images (−0.2 V, 50 pA, 4.7 K) of the same area before (upper) and after (lower) a 5-V voltage pulse is applied for 50 ms on the 1-UC film. The location where the pulse is applied is shown in fig. S16. The arrows indicate the direction of polarization.

the 1-UC one. Both are much lower than that of the bulk material (~10^{13} cm^{-2}). The electronic density of states of 1-UC SnTe film is measured by scanning tunneling spectroscopy (STS). The arrows in the differential conductance (d*I*/d*V*) curve (Fig. 1C) indicate the band edges. The energy gap increases from its bulk value of 0.2 to 1.6 eV in a 1-UC film, mainly originating from the quantum confinement (figs. S23 and S24).

It is challenging to probe the ferroelectric properties of an ultrathin film because of the much-reduced signal compared with the bulk. Usually, more sensitive probes, such as the synchrotron x-ray scattering (*10*), ultraviolet Raman spectroscopy (*12*), polarized second-harmonic generation measurement (*29*), and piezoresponse force microscope (*30*), are employed to detect such weak signals. In our experiment, the small island size requires even more sensitive measurement with high spatial resolution. Here, we use STM and STS to probe the ferroelectricity of SnTe in the 2D limit. The observed evidence for ferroelectricity includes the formation of domain structure (Fig. 1D), lattice distortion (Fig. 1, E and F), band-bending (Fig. 2, A to D), and polarization manipulation by electric field (Fig. 2E).

The domain structure in 1-UC SnTe film is resolved in the STM image (Fig. 1D) at certain sample bias voltage (for example, −0.2 V). The parallel stripes are along the [010] direction. The atomically resolved image (Fig. 1D, left inset) shows a quasi-square lattice of Te atoms (the negative bias corresponds to the filled states mainly contributed by Te). The lattice constant ~ 4.5 Å is in good agreement with the Te-Te distance in the (001) plane of bulk SnTe. The lattice is continuous across the domain boundary (Fig. 1D, left inset). Nevertheless, the Fourier transform of an area containing two domains (STM image in the inset of Fig. 1E) clearly exhibits two sets of Bragg peaks split along the [100] direction (Fig. 1E). Each set of the Bragg peaks is contributed by one domain (see the right panels of Fig. 1E). The lattice is slightly distorted from a perfect square to a parallelogram (Fig. 1F). From the Fourier transform, the two lattice constants of the Te sublattice at liquid helium temperature are found to be 4.58 ± 0.05 and 4.44 ± 0.05 Å, respectively. The parallelogram is elongated along the [110] and its equivalent orientations (indicated by arrows in Fig. 1, D to F). The elongated diagonals for two adjacent domains are perpendicular to each other. As shown later, the in-plane polarization is along those diagonals.

The domain formation and lattice distortion are still not adequate to serve as the conclusive evidence for ferroelectricity. A more direct manifestation comes from the band-bending at the edge of an island. In general, the discontinuity of polarization on the border of a dielectric induces a polarization charge, the density of which is given by $\vec{P} \cdot \vec{n}$. Here, $\vec{P}$ and $\vec{n}$ are the polarization and the normal direction, respectively. If one surface is positively charged, the opposite surface must be negatively charged. The electric field generated by the polarization charge shifts the bulk electronic bands (Fig. 2A). If there are free carriers owing to doping, the screening effect confines the band-bending within the vicinity of the borders (Fig. 2A). Band-bending has various origins and is commonly observed on surfaces. However, the unique feature on the surfaces of ferroelectrics is that the bending directions are opposite to each other on the opposite surfaces of a domain; one side is upward, and the other side is downward (*31*).

The signatures of band-bending can be seen in Fig. 1D. In the STM image (constant current mode at −0.2 V), the height of the island edge is different from that of the bulk, and the edges for two adjacent domains show opposite variation in height. The observed pattern can be easily explained by the band-bending effect if the polarization direction is indeed given by the arrows in Fig. 1D (see also fig. S10). The band gap at an edge is shifted by the polarization charge (Fig. 2B). The positive charge moves the band downward, and there is less density of states between the bias voltage V_s and the Fermi level. Therefore, the apparent height of a positively charged edge is lower than that of the bulk. Similarly, a negatively charged edge appears higher.

The band-bending is even more clearly observed by following the peak at 1.5 V in the d*I*/d*V* curves as a function of the distance to an edge (Fig. 2C). Spatially resolved d*I*/d*V* spectra (right panels) are taken along the lines perpendicular to the edges of two adjacent domains (arrows in the left panel). The peaks shift to opposite directions up to 0.2 eV with a screening length of about 10 nm. For comparison, the d*I*/d*V* mapping is also performed on a 1-UC PbTe island and shows no band-bending effect (fig. S13). PbTe is paraelectric but otherwise is very similar to SnTe.

The above observations do not uniquely determine the orientation of polarization. Any configuration of polarization gives rise to a similar band-bending pattern if the projections of polarization on the normal direction of edge are opposite to each other between two adjacent domains in Fig. 1D. The polarization orientation is unequivocally determined by the band-bending pattern on a single domain island (Fig. 2D). The reversed bending on the opposite edges of the square island clearly demonstrates that the polarization of 1-UC SnTe film has in-plane component along the [110] diagonal.

With the in-plane polarization determined by lattice distortion together with the sign change of polarization charge on edges, we are able to classify the different types of domain walls. The straight domain walls in Fig. 1D belong to the 90° "head-to-tail" type. The "head-to-head" domain wall in Fig. 2E shows the zigzag pattern to

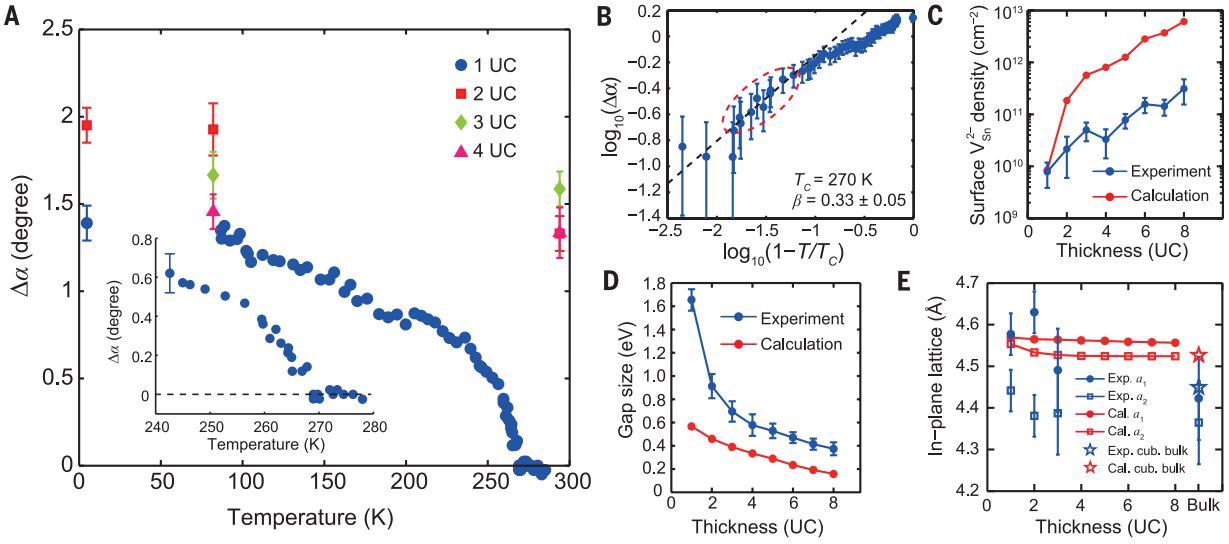

Fig. 3. T_c enhancement in the 1- to 4-UC SnTe films. (**A**) Temperature dependence of the distortion angle for the 1- to 4-UC SnTe films. (Inset) The distortion angle near T_c = 270 K for the 1-UC film exhibiting the behavior of a second-order phase transition. (**B**) Power-law fitting of the data for 1-UC SnTe film near T_c. The critical exponent of P is derived using the approximation $P^2 \propto \Delta\alpha$. The red dashed-line ellipse indicates the data points for linear fitting. (**C**) Thickness dependence of Sn vacancy density at the growth temperature of 450 K. (**D**) Experimentally measured and DFT-calculated thickness dependence of the electronic band gap. The discrepancy between experimental data and DFT calculations comes from the well-known underestimation of band gap in the DFT method (see figs. S23 and S24). (**E**) Thickness dependence of the lattice constants determined by experimental data and DFT calculations (see also fig. S26).

minimize the electrostatic energy (*32*). Occasionally, the in-plane 180° domain wall is also observed (Fig. 2E). More images of domain structures can be found in figs. S14 and S15.

One more important criterion for ferroelectricity is that the polarization can be manipulated by electric field (*32*). A ferroelectric crystal should have two or more orientational states for polarization, which can be shifted from one to another by an electric field. To tune the ferroelectric state, we applied a 5-V voltage pulse between the STM tip and the 1-UC SnTe film. The domain structure of the film is distinctly changed by the pulse (compare the upper and lower panel of Fig. 2E). Here, STM manipulates the ferroelectric polarization through domain wall motion instead of rotation of polarization. The electric field in the tunneling junction is comparable to the typical activation field (~10^7 V/m) for moving a ferroelectric domain wall. Such tunability distinguishes ferroelectric from other polar states.

The above studies, including the formation of domain structure, lattice distortion, band-bending, and polarization manipulation by electric field, strongly support the occurrence of ferroelectricity in the 1-UC SnTe film. However, all the evidence so far is still at the liquid helium temperature. At higher temperatures, the spontaneous polarization $\vec{P}$ diminishes and eventually disappears at the ferroelectric transition temperature T_c, as does the domain structure (fig. S17). During the variable temperature measurement, the distortion angle $\Delta\alpha$ of the rock-salt unit cell is conveniently determined by the separation between the two sets of Bragg peaks (fig. S18). The polarization is then derived through the relation $P^2 \propto \Delta\alpha$ (*33*). The temperature dependence of $\Delta\alpha$ is plotted in Fig. 3A. For the 1-UC film, $\Delta\alpha$ drops as the temperature increases and becomes zero at T_c = 270 K. The critical temperature for 1-UC film is much higher than the bulk value of about 100 K (*25*). Within the precision of measurement, $\Delta\alpha$ approaches zero continuously at T_c (Fig. 3A, inset), which is in agreement with the behavior for a second-order phase transition. The critical index $\beta = 0.33 \pm 0.05$ [$P \sim (T_c - T)^{\beta}$] is extracted by plotting $\Delta\alpha$ versus T on a log-log scale (Fig. 3B). The critical exponent here is identical to the value, 0.33, observed in the $PbZr_{0.9}Ti_{0.1}O_3$ bulk material (*34*) and larger than the values of currently available 2D models with short-range interaction, such as 1/8 of the 2D Ising model (*32*). It indicates that a long-range correlated microscopic model is required to fully account for our observations. From β alone, the universality class of 1-UC SnTe cannot be determined.

For thicker films from 2 to 4 UC, T_c is even higher than the room temperature (RT). Variable-temperature STM measurement above RT is beyond the capability of our current instrument. However, we observed both domain structures and lattice distortion (fig. S19), as well as the band-bending (fig. S20) at RT for 2- to 4-UC films. The evidence for a ferroelectric phase at RT also comes from Raman spectroscopy. The ferroelectric phase transition can be viewed as a condensation of transverse optical (TO) phonon near the Brillouin zone center. Raman spectroscopy directly probes the TO mode softening in ferroelectrics. For SnTe, the Raman signal is inactive above T_c because of the crystalline symmetry of the rock-salt structure. Below T_c, the TO mode becomes Raman active, and its frequency is given by $\omega_{TO} \propto (T_c - T)^{1/2}$ for bulk (*23*). The spectra of 2-UC SnTe film show that the TO mode persists up to RT with only slight softening (fig. S21). For comparison, T_c of the 20-nm-thick film extracted from the TO mode peak shift (fig. S22) is found to be 130 K and consistent with a previous report (*23*).

The strong ferroelectricity enhancement in atomic-layer-thick SnTe films is unusual and may have its origin in the lower free carrier density. The ferroelectric transition strongly depends on the screening effect of free carriers on the dipole-dipole interaction [see (*28*) and fig. S25]. For example, the bulk transition temperature of SnTe reaches 100 K only when the carrier density has been reduced to 10^{20} cm^{-3}. The carrier density depends on the density of defects and the size of the band gap. Both experiment and density functional theory (DFT) calculation (Fig. 3C) reveal that the density of Sn vacancies drops by 2 to 3 orders of magnitude in the SnTe ultrathin film. Besides the lower density of defects, the larger energy gap also helps to make SnTe thin film less conductive. The bulk IV-VI semiconductors such as SnTe usually have narrow band gaps. However, the gap of SnTe is dramatically increased when the film thickness is less than 8 UC (Fig. 3D). The band gap enhancement partially comes from the quantum confinement in the ultrathin film. The T_c of 1-UC film is lower than that of the 2- to 4-UC films, probably because the effects of reduced dimensionality become more prominent in the case of 1 UC.

The in-plane lattice expansion may also facilitate the T_c enhancement. Both experiment (with slightly large uncertainty) and the DFT calculation suggest that the in-plane lattice constants of SnTe increase when the film becomes thinner (Fig. 3E), as generally occurs in the thin film with rock-salt structure (*35*). The lattice constants tune ferroelectricity by adjusting the balance between long-range Coulomb interaction and short-range repulsion (*36*). Such mechanisms may partially

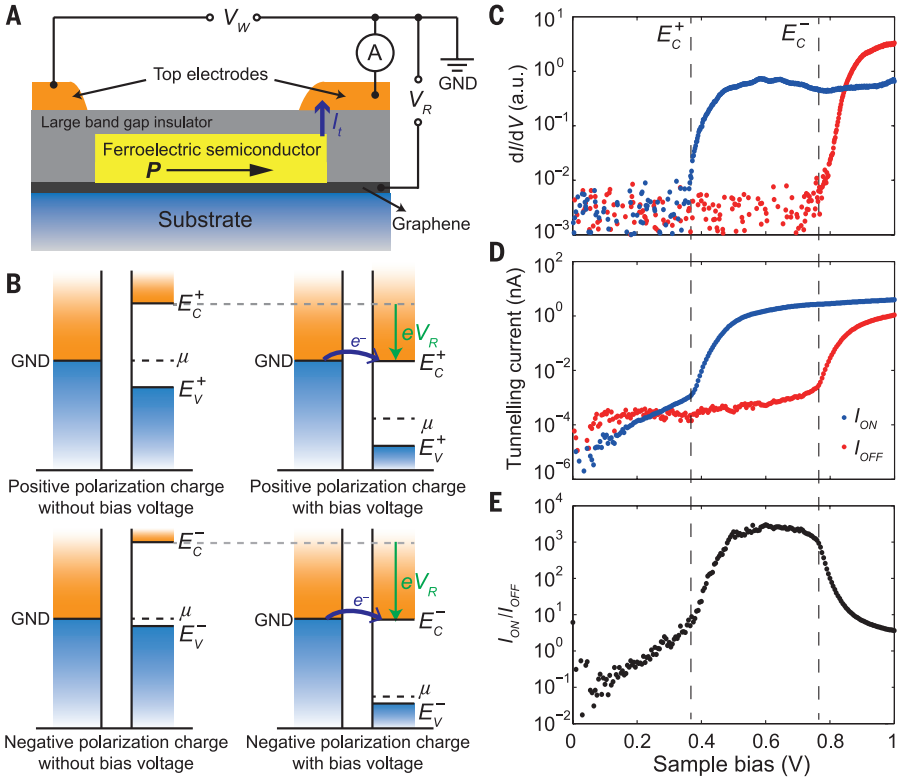

Fig. 4. Proposal for a nonvolatile memory device based on the ferroelectric tunnel junction with in-plane polarization. (**A**) Schematic of the device structure. V_R and V_W are the reading and writing voltages; I_t is the tunneling current. (**B**) Band diagram of the tunneling process between the ferroelectric thin film and a top electrode. μ is the chemical potential of the film. For the positively (negatively) charged state, a threshold voltage $V_R = E_C^+/e(E_C^-/e)$ is needed to open the tunneling channel between the top electrode and the conduction band of the edge. (**C**) Threshold voltages measured by STM. For a 3-UC film, E_C^+ and E_C^- are measured by d*I*/d*V* (set point: 1.0 V, 100 pA) and found to be 0.36 and 0.76 eV, respectively. (**D**) Simulation of the reading process by STM in a 3-UC film. When the tip moves from one edge to another, the feedback loop of STM is turned off to maintain the same distance of tunneling junction. A large on/off ratio is achieved between E_C^+/e and E_C^-/e. (**E**) Bias dependence of the on/off ratio for a 3-UC film obtained from the data in Fig. 4D.

account for the enhancement of ferroelectricity in SnTe and perovskite thin films (*12*, *37*, *38*). In particular, SnTe thin films share several common features with $SrTiO_3/DyScO_3$ (*38*): in-plane lattice expansion, out-of-plane lattice contraction, and in-plane polarization.

Based on the in-plane polarized ferroelectric thin film, a nonvolatile ferroelectric random access memory (FeRAM) device (Fig. 4A) can be designed to take advantage of the small size and high transition temperature. The voltage pulses V_W and V_R are applied only during the writing and reading processes, respectively. The writing voltage V_W generates the in-plane electric field to flip the in-plane polarization of the ferroelectric film. The two opposite directions of polarization represent the "on" and "off" states of the memory unit. The states are read by electron tunneling into an edge driven by the voltage V_R. The tunneling current I_t strongly depends on the band-bending. The dependence can be easily understood by the band structure on the edges (Fig. 4, B and C). To demonstrate the mechanism and simulate the reading process, the *I*-*V* (current-voltage) curves (Fig. 4D) on the edges of a 3-UC SnTe film were measured by STM. During the measurement, the gap distance between tip and sample was fixed. The tunneling current increases rapidly after the bias voltage reaches the corresponding threshold V_R. From 0.5 to 0.7 eV, the on/off ratio can reach as high as 3000 (Fig. 4E). Similar measurement is also performed on 1-UC film, which shows a much lower on/off ratio. Compared with the conventional FeRAM, where reading is destructive, the memory based on the in-plane polarization and tunneling does not reverse the polarization and is nondestructive. Moreover, the fact that ferroelectricity and band-bending could exist in the SnTe nanowire of only 16-nm width (fig. S27) shows the potential to fabricate devices with high density. The materials for insulating layers and electrodes need to be carefully selected for achieving optimal performance.

REFERENCES AND NOTES

1. K. S. Novoselov *et al.*, *Nature* **438**, 197–200 (2005).
2. Y. Zhang, Y.-W. Tan, H. L. Stormer, P. Kim, *Nature* **438**, 201–204 (2005).
3. A. Gozar *et al.*, *Nature* **455**, 782–785 (2008).
4. T. Zhang *et al.*, *Nat. Phys.* **6**, 104–108 (2010).
5. W. Dürr *et al.*, *Phys. Rev. Lett.* **62**, 206–209 (1989).
6. M. Farle, K. Baberschke, *Phys. Rev. Lett.* **58**, 511–514 (1987).
7. X. Xi *et al.*, *Nat. Nanotechnol.* **10**, 765–769 (2015).
8. M. M. Ugeda *et al.*, *Nat. Phys.* **12**, 92–97 (2016).
9. T. Tybell, C. H. Ahn, J.-M. Triscone, *Appl. Phys. Lett.* **75**, 856 (1999).
10. D. D. Fong *et al.*, *Science* **304**, 1650–1653 (2004).
11. D. D. Fong *et al.*, *Phys. Rev. Lett.* **96**, 127601 (2006).
12. D. A. Tenne *et al.*, *Phys. Rev. Lett.* **103**, 177601 (2009).
13. P. Ghosez, K. M. Rabe, *Appl. Phys. Lett.* **76**, 2767 (2000).
14. J. Junquera, P. Ghosez, *Nature* **422**, 506–509 (2003).
15. Z. Wu *et al.*, *Phys. Rev. B* **70**, 104108 (2004).
16. N. Sai, A. M. Kolpak, A. M. Rappe, *Phys. Rev. B* **72**, 020101 (2005).
17. N. Sai, C. J. Fennie, A. A. Demkov, *Phys. Rev. Lett.* **102**, 107601 (2009).
18. Y. Zhang, G.-P. Li, T. Shimada, J. Wang, T. Kitamura, *Phys. Rev. B* **90**, 184107 (2014).
19. E. Almahmoud, I. Kornev, L. Bellaiche, *Phys. Rev. B* **81**, 064105 (2010).
20. A. V. Bune *et al.*, *Nature* **391**, 874–877 (1998).
21. J. O. Dimmock, I. Melngailis, A. J. Strauss, *Phys. Rev. Lett.* **16**, 1193–1196 (1966).
22. N. Wang *et al.*, *Phys. Rev. B* **89**, 045142 (2014).
23. S. Sugai, K. Murase, H. Kawamura, *Solid State Commun.* **23**, 127–129 (1977).
24. W. Jantsch, *Dielectric Properties and Soft Modes in Semiconducting (Pb, Sn, Ge) Te* (Springer, 1983).
25. K. L. I. Kobayashi, Y. Kato, Y. Katayama, K. F. Komatsubara, *Phys. Rev. Lett.* **37**, 772–774 (1976).
26. M. Iizumi, Y. Hamaguchi, K. F. Komatsubara, Y. Kato, *J. Phys. Soc. Jpn.* **38**, 443–449 (1975).
27. T. H. Hsieh *et al.*, *Nat. Commun.* **3**, 982 (2012).
28. See supplementary materials on *Science* Online.
29. Z. Sheng, N. Ogawa, Y. Ogimoto, K. Miyano, *Adv. Mater.* **22**, 5507–5511 (2010).
30. V. Garcia *et al.*, *Nature* **460**, 81–84 (2009).
31. J. L. Giocondi, G. S. Rohrer, *Top. Catal.* **49**, 18–23 (2008).
32. M. E. Lines, A. M. Glass, *Principles and Applications of Ferroelectrics and Related Materials* (Oxford Univ. Press, 1977).
33. R. Clarke, *Phys. Rev. B* **18**, 4920–4926 (1978).
34. R. Clarke, A. M. Glazer, *J. Phys. C Solid State Phys.* **7**, 2147–2156 (1974).
35. F. W. de Wette, W. Kress, U. Schröder, *Phys. Rev. B* **32**, 4143–4157 (1985).
36. G. A. Samara, T. Sakudo, K. Yoshimitsu, *Phys. Rev. Lett.* **35**, 1767–1769 (1975).
37. K. J. Choi *et al.*, *Science* **306**, 1005–1009 (2004).
38. J. H. Haeni *et al.*, *Nature* **430**, 758–761 (2004).

ACKNOWLEDGMENTS

We thank H. J. Xiang, Y. G. Zhao, P. Yu, G. M. Zhang, and B. F. Zhu for helpful discussions. We thank Y. Wang for sample characterization by transition electron microscope and K. Li for helping to prepare substrates. The work is financially supported by National Natural Science Foundation and Ministry of Science and Technology of China. Q.Z. was supported by the Ministry of Science and Technology of China (973 projects 2012CB921701) and the NSF of China. J.L. was supported by the STC Center for Integrated Quantum Materials, NSF Grant No. DMR-1231319. L.F. was supported by the DOE Office of Basic Energy Sciences, Division of Materials Sciences and Engineering under Award No. DE-SC0010526. A provisional patent based on the concept and device in this work has been filed at MIT.

SUPPLEMENTARY MATERIALS

www.sciencemag.org/content/353/6296/274/suppl/DC1
Materials and Methods
Supplementary text
Figs. S1 to S27
Table S1
References (*39*–*51*)

13 November 2015; accepted 16 June 2016
10.1126/science.aad8609

Discovery of robust in-plane ferroelectricity in atomic-thick SnTe

Kai Chang, Junwei Liu, Haicheng Lin, Na Wang, Kun Zhao, Anmin Zhang, Feng Jin, Yong Zhong, Xiaopeng Hu, Wenhui Duan, Qingming Zhang, Liang Fu, Qi-Kun Xue, Xi Chen and Shuai-Hua Ji

(July 14, 2016)
Science **353** (6296), 274-278. [doi: 10.1126/science.aad8609]

Editor's Summary

Thinning a ferroelectric makes it better

As a ferroelectric material becomes thinner, the temperature below which it develops its permanent electrical polarization usually decreases. Chang *et al.* fabricated high-quality thin films of SnTe that, in contrast to this conventional wisdom, had a considerably higher transition temperature than that of the material in bulk (see the Perspective by Kooi and Noheda). This was true even for single-unit cell films, whereas only slightly thicker films became ferroelectric above room temperature. This finding may enable the miniaturization of ferroelectric devices.

Science, this issue p. 274; see also p. 221

Science (print ISSN 0036-8075; online ISSN 1095-9203) is published weekly, except the last week in December, by the American Association for the Advancement of Science, 1200 New York Avenue NW, Washington, DC 20005.